

# Effect of the Interpass Temperature on Simulated Heat-Affected Zone of Gas Metal Arc Welded API 5L X70 Pipe Joint

Paulo Henrique Grossi Domelas (✉ [pdomelas@metalmat.ufrj.br](mailto:pdomelas@metalmat.ufrj.br))

Universidade Federal do Rio de Janeiro

João da Cruz Payão Filho

Universidade Federal do Rio de Janeiro

Victor Hugo Pereira Moraes e Oliveira

Universidade Federal do Rio de Janeiro

Diogo de Oliveira Moraes

São José dos Campos – SP, Brazil

Petrônio Zumpano Júnior

São José dos Campos – SP, Brazil

---

## Research Article

**Keywords:** coarse grain heat-affected zone, intercritically reheated coarse-grain heat-affected zone, finite element method, thermodynamic simulation, physical simulation

**Posted Date:** September 3rd, 2021

**DOI:** <https://doi.org/10.21203/rs.3.rs-864136/v1>

**License:**  This work is licensed under a Creative Commons Attribution 4.0 International License.

[Read Full License](#)

---

**Version of Record:** A version of this preprint was published at The International Journal of Advanced Manufacturing Technology on October 28th, 2021. See the published version at <https://doi.org/10.1007/s00170-021-08261-2>.

# Abstract

Welding costs associated with the laying of pipes for deepwater oil and gas extraction can be reduced using high interpass temperatures (ITs). However, a high IT can decrease the mechanical properties of the heat-affected zone (HAZ) of welded joints. With the use of high strength-toughness steels, this decrease may be an acceptable trade-off. Therefore, it is necessary to evaluate the influence of high ITs on the HAZ. The influence of the IT on the coarse grain HAZ (CGHAZ) and intercritically reheated coarse-grain HAZ (ICCGHAZ) of an API 5L X70 pipe joint welded by gas metal arc welding was investigated. The welding was numerically simulated using finite element method software. The microstructure of the HAZ was predicted using thermodynamic simulation software. The CGHAZ and ICCGHAZ were also physically simulated and evaluated via optical microscopy and scanning electron microscopy, dilatometry, and Vickers microhardness and Charpy V-notch (CVN) impact tests. The increase in IT led to a decrease in CGHAZ microhardness, but did not affect the ICCGHAZ. The CVN energies obtained for all ITs (CGHAZ and ICCGHAZ) were higher than that set by the DNVGL-ST-F101 standard (50 J). These results show that increasing the IT is an interesting and effective method to reduce welding costs. In addition, thermodynamic simulation proved to be a valid method for predicting the phases in the HAZ of API 5L X70 pipe welded joints.

## 1. Introduction

To strengthen their position in a highly competitive market, oil and gas companies have funded research projects aimed at developing solutions to reduce their process costs. The exploration of oil and gas in high-deep-water requires the use of longer rigid risers. These pipes are initially welded on support ships (~ US \$650,000/day rent) and then laid by the J-lay method. One way to reduce the costs of installing pipes in deep water is to reduce the welding time. The reduction of the welding time can be achieved by developing welding parameters, such as high heat input [1] and welding current [2]. However, this can decrease the hardness and impact toughness [3–4] of the heat-affected zone (HAZ) of high-strength low-alloy (HSLA) steels because of the formation of brittle regions, such as a coarse grain HAZ (CGHAZ) [5] and an intercritically reheated coarse-grain HAZ (ICCGHAZ) [6], which increase the risk of welded joint failure [7].

Another method that has been studied is the use of a high welding interpass temperature (IT), which reduces the time required for joint cooling, thus increasing productivity. Sirin et al. [8] observed that intermittent welding (with interruptions for joint cooling) increased the fracture toughness of the welded joint by approximately 18% compared with a continuous process. They concluded that the IT directly influenced the toughness of the HAZ of an API 5L X65 pipe. However, Neves and Loureiro [9] reported that a high IT reduces the HAZ fracture toughness, compromising the performance of the welded joint in service. The increase in IT reduces the cooling rate of the welded joint owing to the lower temperature gradient in the HAZ [10]. Shi and Han [11] reported a drop in the HAZ toughness owing to the amount of martensite-austenite (M-A) constituents formed at lower cooling rates. Dornelas et al. [12] observed that the increase in the IT significantly changed in the microstructure, and consequently decreased the CGHAZ

hardness and fracture toughness of a Cr-Mo low-alloy steel. On the other hand, Wang et al. [13] reported an improvement in the HAZ toughness due to an increase in IT between 80°C and 130°C; however, a drop was observed when the IT increased beyond 130°C. Therefore, the use of a higher IT seems to be critical in alloys sensitive to the cooling rate, justifying its control to ensure good fracture toughness. Steels with high fracture toughness may lose some of their properties without compromising their performance during service, thus reducing production costs. Thus, it is necessary to study the influence of an increase in IT on the CGHAZ and ICCHAZ of these alloys.

In welding with different parameters from those specified by the welding procedure (e.g., higher IT), it is necessary to perform a series of tests to evaluate the mechanical behavior of the welded joint, followed by a requalification of the new parameters, which is expensive. In this case, computer simulations of the welding process and thermodynamic simulations can be used to predict the HAZ thermal cycles and microstructures under different welding conditions (e.g., IT); this speeds up the analysis and makes it less expensive. Computer simulations of welding (finite element method, FEM) [14–18] and thermodynamics (Calphad method) [12, 19–20] have developed in recent years.

To reduce welding costs, this paper examines the effects of welding at  $IT \geq 300^\circ\text{C}$  on the microstructures and impact toughness of the simulated CGHAZ and ICCGHAZ of a high strength-toughness API 5L X70 pipe. The welding thermal cycles of the CGHAZ and ICCGHAZ were simulated using a commercial FEM software. Then, the CGHAZ and ICCGHAZ were evaluated by optical microscopy (OM), scanning electron microscopy (SEM), and Vickers microhardness and Charpy V-notch (CVN) impact tests. The simulated welding thermal cycles were also reproduced in dilatometry tests. A commercial thermodynamic simulation software (Calphad method) was used to predict the CGHAZ and ICCGHAZ microstructures. A comparative study was performed to evaluate the accuracy of the predictions.

## 2. Materials And Methods

### 2.1. Materials

A hot-rolled (seamless, Mannesmann process) HSLA API 5L X70 pipe with a ferritic microstructure (Fig. 1) was welded in this work. Table 1 lists the chemical compositions (wt. %) of the pipe and weld metal. Table 2 lists the mechanical properties of the pipe. The carbon equivalent (CEIIW) was calculated from Eq. 1.

Table 1  
 Chemical compositions (wt. %) of the API 5L X70 pipe and weld metal analyzed by optical emission spectroscopy, and the carbon equivalent ( $CE_{IIW}$ ) of the API 5L X70 pipe.

Chemical element	Material	
	API 5L X70 pipe	Weld metal
C	0.019	0.071
Mn	1.397	1.430
Si	0.254	0.710
P	0.010	0.015
S	0.002	0.011
Cr	0.023	0.048
Mo	0.057	0.017
Ni	0.148	0.027
Nb + V + Ti	0.080	< 0.012
Al	0.028	0.004
Cu	0.475	0.106
$CE_{IIW}$	0.32	□

$$CE_{IIW} = C + \frac{Mn}{6} + \frac{(Cr + Mo + V)}{5} + \frac{(Cu + Ni)}{15}$$

1

Table 2  
 Mechanical properties of the API 5L X70 pipe and weld metal.

Mechanical property	Pipe	Weld metal (specified)
Ultimate tensile strength, UTS [MPa]	575	583
Yield strength, YS [MPa]	540	483
Elongation, El. [%]	61	26
Charpy V-notch impact energy (at - 30 °C), CVN [J]	293	□
Vickers microhardness, HV1	193	□

## 2.2. Gas metal arc welding

The API 5L X70 pipe was gas metal arc girth welded to obtain the data to be used as input in the numerical simulation and to perform its validation. Table 3 presents the parameters adopted for gas metal arc welding. Figure 2 shows the groove configuration and a schematic of the weld passes performed.

Table 3  
Parameters adopted in the gas metal arc welding of the API 5L X70 pipe.

Parameter	Welding pass			
	Root	Hot	Fill	Cap
Arc voltage, U [V]	13–19	25–31	25–31	14–22
Welding current, I [A]	132–180	239–337	239–298	126–220
Welding speed, WS [ $\text{cm} \cdot \text{min}^{-1}$ ]	22–30	34–42	32–47	35–44
Heat input, HI [ $\text{kJ} \cdot \text{mm}^{-1}$ ]	0.6–1.0	1.0–1.6	0.9–1.4	0.3–0.7
Welding current type and polarity	DC +			
Welding position	2G			
Filler metal	AWS A5.18 ER70S-6			
Shielding gas type	80% Ar + 20% CO <sub>2</sub>			
Shielding gas flow rate [ $\text{L} \cdot \text{min}^{-1}$ ]	20–33			
Preheating temperature, T <sub>o</sub> [°C]	90			
Interpass temperature, IT [°C]	245			

## 2.3. Welding modeling

To describe the HAZ thermal cycles, the physical welding thermal cycle simulators used simplified analytical models such as Rosenthal [21] and Rykalin 2D [22]. These models simplified some factors; for example, the physical properties are temperature-independent, the metals are solid during welding, no solid phase transformation occurs, there is no heat loss by radiation and convection, and the heat source has zero volume (point or line) [23]. However, these simplifications lead to errors in the HAZ thermal cycle simulation. Numerical simulation methods (e.g., FEM) have been used to overcome these limitations and make the physical simulation more realistic [24–25]. The commercial FEM software Sysweld® was used to accurately describe the CGHAZ and ICCGHAZ thermal cycles. The weld metal elements were simulated using the birth and death technique. The procedures for executing, documenting, and validating the welding simulations followed the ISO 18166 standard.

The welding was modeled using the principle of energy conservation [26]. The fundamental equation of heat conduction in multiphase solids is expressed as Eq. 2, where the temperature distribution ( $T$ ) is a function of the time ( $t$ ) and position ( $x, y, z$ ).  $k$  is the thermal conductivity,  $c_p$  is the specific heat,  $\rho$  is the density,  $T$  is the temperature distribution,  $P$  is the phase proportion, and  $\dot{Q}$  is the heat generated per volume.  $i$  and  $j$  are phases indexes,  $A_{ij}$  is the proportion of phase transformation per unit time, and  $L_{ij}(T)$  is the latent heat of the phase transformation.  $c_p$ ,  $k$ , and  $\rho$  (Table 4) are obtained from the chemical composition-based thermodynamic simulation of the pipe using the JMatPro<sup>®</sup> software. The same properties were used for the base and weld metals during the simulation because their chemical compositions were similar.

$$\frac{\partial}{\partial x} \left( \left( \sum_i P_i(T) \right) k_i(T) \frac{\partial T}{\partial x} \right) + \frac{\partial}{\partial y} \left( \left( \sum_i P_i(T) \right) k_i(T) \frac{\partial T}{\partial y} \right) + \frac{\partial}{\partial z} \left( \left( \sum_i P_i(T) \right) k_i(T) \frac{\partial T}{\partial z} \right) + \dot{Q} - \sum_{i < j} A_{ij} L_{ij}(T) = \rho \sum_i P_i(T) c_{p,i} \frac{\partial T}{\partial t}$$

Table 4  
Density ( $\rho$ ), thermal conductivity ( $k$ ), and specific heat ( $c_p$ ) of the HSLA API 5L X70 pipe at a constant pressure and various temperatures (T).

Temperature, T [°C]	Density, $\rho$ [g·cm <sup>-3</sup> ]	Thermal conductivity, $k$ [W·(m·K) <sup>-1</sup> ]	Specific heat, $c_p$ [J·(g·K) <sup>-1</sup> ]
2000	6.58	42.92	0.82
1900	6.67	41.07	0.82
1800	6.75	39.23	0.82
1700	6.84	37.38	0.82
1600	6.92	35.54	0.82
1500	7.25	35.45	0.73
1400	7.33	34.33	0.69
1300	7.38	33.11	0.67
1200	7.44	31.89	0.66
1100	7.49	30.66	0.64
1000	7.55	29.45	0.63
900	7.60	28.23	0.61
800	7.59	30.38	0.96
700	7.61	32.81	0.98
600	7.64	35.01	0.82
500	7.68	37.54	0.69
400	7.72	40.03	0.62
300	7.75	42.03	0.56
200	7.78	43.15	0.52
100	7.82	43.10	0.48
25	7.84	42.21	0.45

The initial condition of the model assumed an IT of 245°C at 25 mm away from the groove (a common measurement location in welding). The IT is heterogeneous in the joint owing to the localized heating induced by the electric arc [27]; hence, the model considers the temperature distribution as the initial condition. The boundary condition considers the heat flow due to convection and radiation in the welded joint according to Eq. 3, where  $q$  is the energy supplied by the heat source,  $\varepsilon$  is the emissivity coefficient

(0.8),  $\sigma$  is the Stefan–Boltzmann constant ( $5.6704 \cdot 10^{-8} \text{ Wm}^{-2}\text{K}^{-4}$ ),  $T_0$  is the room temperature ( $20^\circ\text{C}$ ), and  $h$  is the convective heat transfer coefficient ( $25 \text{ Wm}^{-2}\text{K}^{-4}$ ). The latent heat of the phase transformation is also considered.

$$-k \left( \frac{\partial T}{\partial x} + \frac{\partial T}{\partial y} + \frac{\partial T}{\partial z} \right) = q - \epsilon \sigma (T^4 - T_0^4) - h (T - T_0)$$

3

The moving Goldak double-ellipsoid model [28] was adopted to represent the welding heat source. This model is a combination of two ellipsoids, one in front and the other at the rear, as described by Eq. 4.  $a$ ,  $b$ , and  $c_i$  are the semi-axes of the double ellipsoid (Table 5);  $v$ ,  $q_i$  and  $t$  are the welding speed (Table 3), power density distribution in the double ellipsoid, and time, respectively.  $U$  is the electric arc voltage,  $\eta$  is the thermal efficiency of welding (0.86), and  $I$  is the welding current (Table 3).  $r$  and  $f$  are the rear and front quadrants of the Goldak double ellipsoid;  $f_r$  and  $f_f$  are the fractions of the heat at the rear ( $f_r$ , Table 5) and front ( $f_f = 2 - f_r$ ), respectively. Table 5 presents the dimensions of Goldak's heat source (I and II) used to simulate the weld passes 7–8 (I) and 5–6 (II). Figure 2 shows the weld pass numbers 5–8.

$$q_i(x, y, z, t) = \frac{6\sqrt{3}f_i\eta UI}{abc_i\pi\sqrt{\pi}} \exp \left( -3\frac{x^2}{a^2} - 3\frac{y^2}{b^2} - 3\frac{(z - vt)^2}{c_i^2} \right), i = f \text{ and } r$$

4

Table 5  
Goldak's heat source parameters.

Heat source	$a$	$b$	$c_f$	$c_r$	$f_f$
I	3.50	2.50	6.00	6.00	1.09
II	3.00	1.00	1.15	3.85	1.20

The accuracy of an FEM model is influenced by the mesh density used in the physical analysis. Thus, it is necessary to perform mesh refinement in the study regions (CGHAZ and ICCGHAZ) because they experienced severe temperature gradients during welding. The adequate meshing for the problem was based on the literature [29] and the authors' simulation experience. Figure. 3 presents the FEM model mesh and a macrograph of the welded joint. Figure. 4 shows the thermal profile during the welding simulation of the sixth pass (forming a CGHAZ – left) and the eighth pass (forming a CGHAZ and ICCGHAZ – right). The ICCGHAZ was formed because of the intercritical reheating ( $900-773^\circ\text{C}$ ) of the previous CGHAZ.

## 2.4. Physical simulation of the CGHAZ and ICCGHAZ

The simulated CGHAZ and ICCGHAZ welding thermal cycles (Sect. 3.1) were reproduced in the specimens using a Gleeble® 3800 physical simulator. The specimens (11 mm × 11 mm × 80 mm) were removed along the longitudinal direction of the pipe. After the physical simulation, these were subjected to microscopy, Vickers microhardness measurements, and Charpy V-notch impact testing.

## 2.5. Thermodynamic simulation

Thermodynamic simulation was performed using the JMatPro® software to obtain the physical properties of the API 5L X70 pipe (Table 4) and the continuous cooling transformation (CCT) diagram (Fig. 5). To predict the microstructures, simulations of the phase contents during cooling for all ITs (CGHAZ and ICCGHAZ) using the average cooling rate as the input data were performed. The average cooling rate was calculated as 1350–300°C (CGHAZ) for IT = 300, 350, 400, and 425°C (9, 4.6, 2.9, and 2.6°C/s, respectively) from the simulated thermal welding cycles (Sect. 3.1). For the ICCGHAZ, the average cooling rate was similar for all conditions (1°C/s, owing to the lower peak temperature, 850°C); hence, only a single simulation was performed for all ITs. All the previously mentioned simulations were based on the chemical composition of the base metal (Table 1).

## 2.6. Dilatometry

Dilatometry tests were performed using the CGHAZ and ICCGHAZ simulated welding thermal cycles (Sect. 3.1) in a Gleeble 3800 physical simulator. The well-known tangent method [30] was applied to determine the phase formation starting temperatures during cooling.

## 2.7. Microstructural characterization

The physically simulated specimens were microstructurally characterized by OM (Zeiss Axio Imager M2m) and SEM (Tescan VEJA 3). The OM and SEM specimens were ground (sandpaper from 100 to 1200 grade), polished (diamond paste from 3 to 1 µm), and etched with 2% nital followed by 2% picral solutions.

## 2.8. Mechanical testing

Full-size CVN impact testing was performed using a JBW-300 pendulum impact tester at -30°C, in accordance with ASTM A370. The microhardness test was performed using an HV-1000 Digimet hardness tester with a load of 1 kgf, in accordance with ASTM E92.

# 3. Results And Discussion

## 3.1. FEM model and its validation

The welding simulation was validated by comparing the simulated welding thermal cycles (Sysweld®) in the last four weld passes with the actual thermal cycles measured with thermocouples; both were

obtained from the base metal 25 mm away from the joint groove. A similar validation procedure is specified in ISO 18166, which has been used by other authors in the literature [4, 12, 31]. Figure 6 shows the excellent correlation between the simulated and measured welding thermal cycles. After validation of the FEM model, welding simulations were performed considering the ITs of 300, 350, 400, and 425°C. Figure 7 shows the thermal cycles obtained for the CGHAZ and ICCGHAZ.

## 3.2. Microstructural characterization

Figure 8 shows the macrographs of the simulated CGHAZ. For IT = 300°C, the CGHAZ was formed by needle ferrite and massive and slender aligned martensite-austenite-carbide (M-A-C) morphologies, which were also observed by Di et al. [32] and Zhu et al. [33]. For IT  $\geq$  350°C, the ferritic grains were larger and only massive M-A-C formed compared with IT = 300°C. Needle ferrite was formed for IT = 300°C because of the shorter time available (i.e., with thermodynamically favorable conditions) for the diffusion of alloying elements, and consequently grain growth. This behavior occurred because of the higher cooling rate of the alloy during its phase transformation at 850–400°C (CCT diagram in Fig. 6) for IT = 300°C compared with the other ITs (Fig. 9). According to the literature [34–36], the increase in heat input changes the M-A-C morphology from slender to massive owing to the decrease in the cooling rate. Figures 8 and 9 show that the IT increase decreased the cooling rate, creating the necessary thermodynamic conditions for the formation of a massive instead of slender M-A-C. The microstructures observed in the CGHAZ were similar to those observed by other researchers [32–33, 37–38], although some have also identified the formation of granular bainite [37, 39]. The phase content during cooling, obtained from the thermodynamic simulation (Fig. 10), indicate the presence of ferrite for all ITs. For IT  $\geq$  350°C, the minor formation of perlite and bainite was predicted (< 1%). The formation of ferrite for all ITs was confirmed by dilatometry tests (Fig. 11).

Figure 12 shows micrographs of the simulated ICCGHAZ. For IT = 300°C, ferrite and massive M-A-C were formed. However, owing to intercritical reheating, the ferritic grains were equiaxial and larger than those in the CGHAZ. For IT  $\geq$  350°C, M-A-C formation was observed at the grain boundaries of the prior austenite, which was also observed by other authors [40–41]. The grain boundary M-A-C observed for IT  $\geq$  350°C may be related to the lower cooling rate after intercritical reheating (Fig. 9), which can produce the thermodynamically favorable conditions for the diffusion of alloying elements over a longer period. The formation of ferrite for all ITs was confirmed by dilatometry tests (Fig. 13). The thermodynamic simulation (JMatPro<sup>®</sup>) indicated the major presence of ferrite (Fig. 14) and minor perlite (< 1%) for all ITs.

From the microstructural analysis and dilatometry, it was possible to obtain good agreement between the observed and predicted microstructures in the CGHAZ and ICCGHAZ for all ITs. These results show that thermodynamic simulation for phase prediction is a valid and powerful method for analyzing the welding of API 5L X70 pipes.

## 3.3. Mechanical testing

Figure 15 shows the Vickers microhardness values of the CGHAZ and ICCGHAZ. For the CGHAZ, the increase in IT led to a decrease in microhardness owing to the reduction of the cooling rate (Fig. 9). Such

thermodynamically favorable conditions promoted greater diffusion of the alloying elements, thus decreasing the hardening by solid solution in the resulting ferritic microstructure. This difference in diffusion explains the change in the needle to equiaxial ferrite, as previously reported (Sect. 3.2). The decrease in microhardness with the reduction in cooling rate was also observed in other studies [4, 37, 42]. For the ICCGHAZ, the increase in IT did not strongly influence the Vickers microhardness because the cooling rates arising from the different ITs are similar (Fig. 9b).

The CVN energies for all ITs, for both the CGHAZ and ICCGHAZ, reached the maximum value of the equipment (300 J), i.e., the specimens did not fracture. The high CVN energies are attributed to the maintenance of the ferritic microstructure in all cases. Figures 8 and 12 show that in both the CGHAZ and ICCGHAZ, M-A-C was formed with slender and massive morphologies [34, 43]. Several studies have investigated the influence of the M-A-C morphology on the toughness. Despite the controversy over whether the slender [34, 44] or massive [45–46] morphology is more detrimental to toughness, all studies agree that both morphologies can cause the HAZ of the API 5L X70 pipe to become brittle [32, 40, 47]. Because of the high CVN energies obtained, it was not possible to assess the influence of M-A-C formation. However, even if this influence is negative, the obtained CVN energies were considerably higher than the limit set by the DNVGL-ST-F101 standard (50 J). Thus, all the investigated ITs do not jeopardize the fracture toughness of the HAZ.

## 4. Conclusions

In this study, the influence of the IT on the numerically and physically simulated CGHAZ and ICCGHAZ of an API 5L X70 pipe was studied. The increase in IT decreased the Vickers microhardness of the CGHAZ owing to lower cooling rates. For the ICCGHAZ, the influence of the IT was weaker. Despite the formation of M-A-C in the CGHAZ and ICCGHAZ, the CVN impact energies in these regions were considerably higher than the limit set by the DNVGL-ST-F101 standard (50 J). These results show that a high IT can reduce the welding time and increase productivity. Moreover, the thermodynamic simulation proved to be an efficient method for predicting the HAZ microstructure of API 5L X70 pipe, reducing costs through tests and analyses.

## Declarations

**Authors' contributions:** Formal analysis, P.H.G.D., V.H.P.M.O., and J.d.C.P.F.; funding acquisition, D.O.M., P.Z.J., and J.d.C.P.F.; investigation: P.H.G.D.; method: P.H.G.D.; and V.H.P.M.O.; project administration: D.O.M., P.Z.J., and J.d.C.P.F.; supervision, D.O.M., P.Z.J., and J.d.C.P.F.; original draft, P.H.G.D. and V.H.P.M.O.; writing-review and editing, P.H.G.D., J.d.C.P.F., V.H.P.M.O., D.O.M., and P.Z.J.

**Funding:** This work was funded by Petróleo Brasileiro S. A. (Petrobras) and Agência Nacional do Petróleo, Gás Natural e Biocombustíveis (ANP) – grant 2016/00335-0.

**Conflict of interest:** The authors declare no conflict of interest.

**Data availability:** The raw/processed data required to reproduce these findings cannot be shared at this time as the data also forms part of an ongoing study.

## References

1. Barbosa LHS, Modenesi PJ, Godefroid LB, Arias AR (2019) Fatigue crack growth rates on the weld metal of high heat input submerged arc welding. *Int J Fatigue* 119:43–51. doi:10.1016/j.ijfatigue.2018.09.020
2. Layus P, Kah P, Martikainen J, Gezha VV, Bishokov RV (2014) Multi-wire SAW of 640 MPa Arctic shipbuilding steel plates. *Int J Adv Manuf Technol* 75:771–782. doi:10.1007/s00170-014-6147-2
3. Li L, Han T, Han B (2018) Embrittlement of intercritically reheated coarse grain heat-affected zone of ASTM 4130 steel. *Metall Mater Trans A Phys Metall Mater Sci* 49:1254–1263. doi:10.1007/s11661-018-4480-z
4. Dornelas PHG, Farias FWC, Oliveira VHPM, Moraes DO, Zumpano Júnior P, Payão Filho JC (2020) Influence of welding interpass temperature on Charpy V-notch impact energy of coarse-grain heat-affected zone of AISI 4130 steel pipe. *Int J Adv Manuf Technol* 108:2197–2211. doi:10.1007/s00170-020-05542-0
5. Arora KS, Pandu SR, Shajan N, Pathak P, Shome M (2018) Microstructure and impact toughness of reheated coarse grain heat affected zones of API X65 and API X80 linepipe steels. *Int J Press Vessel Pip* 163:36–44. doi:10.1016/j.ijpvp.2018.04.004
6. Qi X, Di H, Wang X, Liu Z, Misra RDK (2020) Effect of secondary peak temperature on microstructure and toughness in ICCGHAZ of laser-arc hybrid welded X100 pipeline steel joints. *Integr Med Res* 9:7838–7849. doi:10.1016/j.jmrt.2020.05.016
7. Shackleton DN (2006) Reducing failure risk in welded components. *Riv Ital della Saldatura* 58:79–83. doi:10.1007/BF03263449
8. Sirin K, Sirin SY, Kaluc E (2016) Influence of the interpass temperature on t<sub>8/5</sub> and the mechanical properties of submerged arc welded pipe. *J Mater Process Technol* 238:152–159. doi:10.1016/j.jmatprotec.2016.07.008
9. Neves J, Loureiro A (2004) Fracture toughness of welds - Effect of brittle zones and strength mismatch. *J Mater Process Technol* 153:537–543. doi:10.1016/j.jmatprotec.2004.04.120
10. Muthupandi V, Srinivasan PB, Seshadri SK, Sundaresan S (2003) Effect of weld metal chemistry and heat input on the structure and properties of duplex stainless steel welds. *Mater Sci Eng A* 358:9–16. doi:10.1016/S0921-5093(03)00077-7
11. Shi Y, Han Z (2008) Effect of weld thermal cycle on microstructure and fracture toughness of simulated heat-affected zone for a 800 MPa grade high strength low alloy steel. *J Mater Process Technol* 207:30–39. doi:10.1016/j.jmatprotec.2007.12.049
12. Dornelas PHG, Farias FWC, Oliveira VHPM, Moraes DO, Zumpano Júnior P, Payão Filho JC (2020) FEM-thermodynamic simulation methodology to predict the influence of t<sub>8/5</sub> on the coarse grain

- heat-affected zone of a Cr-Mo low-alloy steel pipe. 60:520–529. doi: 10.1016/j.jmapro.2020.10.082
13. Wang XL, Tsai YT, Yang JR, Wang ZQ, Li XC, Shang CJ, Misra RDK (2017) Effect of interpass temperature on the microstructure and mechanical properties of multi-pass weld metal in a 550-MPa-grade offshore engineering steel. *Weld World* 61:1155–1168. doi:10.1007/s40194-017-0498-x
  14. Toyoda M, Mochizuki M (2004) Control of mechanical properties in structural steel welds by numerical simulation of coupling among temperature, microstructure, and macro-mechanics. *Sci Technol Adv Mater* 5:255–266. doi:10.1016/j.stam.2003.10.027
  15. Wongpanya P, Boellinghaus T, Lothongkum G, Kannengiesser T (2008) Effects of preheating and interpass temperature on stresses in S 1100 QL multi-pass butt-welds. *Weld World* 52:79–92. doi:10.1007/BF03266634
  16. Novotný L, Abreu HFG, Miranda HC, Béréš M (2016) Simulations in multipass welds using low transformation temperature filler material. *Sci Technol Weld Join* 21:680–687. doi:10.1080/13621718.2016.1177989
  17. Dai H, Moat RJ, Withers PJ (2011) Modelling the interpass temperature effect on residual stress in low transformation temperature stainless steel welds. *Am Soc Mech Eng Press Vessel Pip Div PVP* 6:1451–1458. doi:10.1115/PVP2011-57329
  18. Zubairuddin M, Albert SK, Vasudevan M, Mahadevan S, Chaudhri V, Suri VK (2016) Thermomechanical analysis of preheat effect on grade P91 steel during GTA welding. *Mater Manuf Process* 31:366–371. doi:10.1080/10426914.2015.1025964
  19. Miettinen J, Koskenniska S, Visuri V (2020) Thermodynamic, kinetic, and microstructure data for modeling solidification of Fe-Al-Mn-Si-C alloys. 51: 2946–2962. doi: 10.1007/s11663-020-01973-y
  20. Kohler ML, Kunz J, Herzog S, Kaletsch A, Broeckmann C (2021) Microstructure analysis of novel LPBF-processed duplex stainless steels correlated to their mechanical and corrosion properties. 801:140432. doi: 10.1016/j.msea.2020.140432
  21. Rosenthal D (1941) Mathematical theory of heat distribution during welding and cutting. *Weld J* 20:220–234
  22. Goldak J, Bibby M, Moore J, House R, Patel B (1986) Computer modeling of heat flow in welds. *Metall Trans B* 17:587–600. doi:10.1007/BF02670226
  23. Myers PS (1976) Fundamentals of heat flow in welding. Welding Research Council
  24. Anca A, Cardona A, Risso J, Fachinotti VD (2011) Finite element modeling of welding processes. *Appl Math Model* 35:688–707. doi:10.1016/j.apm.2010.07.026
  25. Pozo-Morejón JA, Souza LF, Guerra T, Morales EV, Bott IDS, Cruz-Crespo A, Pérez OR (2018) Ajuste de los calores de entrada que se corresponden con los tiempos de enfriamiento de la ZAT en soldadura GMAW sobre acero dúplex 2205 empleando la simulación por elementos finitos. *Sold Insp* 23:413–422. doi:10.1590/0104-9224/si2303.10
  26. Kik T, Górká J (2019) Numerical simulations of laser and hybrid S700MC T-joint welding. *Materials* 12:516. doi:10.3390/ma12030516

27. Geng H, Li J, Xiong J, Lin X (2017) Optimisation of interpass temperature and heat input for wire and arc additive manufacturing 5A06 aluminium alloy. *Sci Technol Weld Join* 22:472–483. doi:10.1080/13621718.2016.1259031
28. Goldak J, Chakravarti A, Bibby M (1984) A new finite element model for welding heat sources. *Metall Trans* 15:299–305. doi:10.1007/BF02667333
29. Heinze C, Schwenk C, Rethmeier M (2011) Influences of mesh density and transformation behavior on the result quality of numerical calculation of welding induced distortion. *Simul Model Pract Theory* 19:1847–1859. doi:10.1016/j.simpat.2011.05.001
30. Harrison PL, Farrar RA (1989) Application of continuous cooling transformation diagrams for welding of steels. *Int Mater Rev* 34:35–51. doi:10.1179/imr.1989.34.1.35
31. Bate SK, Charles R, Warren A (2009) Finite element analysis of a single bead-on-plate specimen using Sysweld. *Int J Press Vessels Pip* 86:73–78. doi:10.1016/j.ijpvp.2008.11.006
32. Di XJ, An X, Cheng FJ, Wang DP, Guo XJ, ue ZK (2016) Effect of martensite–austenite constituent on toughness of simulated inter-critically reheate coarse-grained heat-affected zone in X70 pipeline steel. *Sci Technol Weld Join* 21:366–373. doi:10.1080/13621718.2015.1118814
33. Zhu Z, Han J, Li H (2015) Effect of alloy design on improving toughness for X70 steel during welding. *Mater Des* 88:1326–1333. doi:10.1016/j.matdes.2015.09.073
34. Luo X, Chen X, Wang T, Pan S, Wang Z (2017) Effect of morphologies of martensite–austenite constituents on impact toughness in intercritically reheated coarse-grained heat-affected zone of HSLA steel. *Mater Sci Eng A* 710:192–199. doi:10.1016/j.msea.2017.10.079
35. Yang X, Di X, Liu X, Wang D, Li C (2019) Effects of heat input on microstructure and fracture toughness of simulated coarse-grained heat affected zone for HSLA steels. *Mater Charact* 155:109818. doi:10.1016/j.matchar.2019.109818
36. Zhuangfei W, Minghao SHI, Shuai T, Guodong W (2017) Effect of heat input and M-A constituent on microstructure evolution and mechanical properties of heat affected zone in low carbon steel. *J Wuhan Univ Technol Mater Sci Ed* 32:1163–1170. doi:10.1007/s11595-017-1726-3
37. Li C, Wang Y, Han T (2011) Microstructure and toughness of coarse grain heat-affected zone of domestic X70 pipeline steel during in-service welding. *J Mater Sci* 46:727–733. doi:10.1007/s10853-010-4803-y
38. Li CW, Wang Y, Han T (2012) Toughness improvement in coarse grain heat affected zone of X70 pipeline steel by accelerated cooling. *Mater Sci Technol* 28:92–94. doi:10.1179/1743284711Y.0000000002
39. Li C, Wang Y, Chen Y (2011) Influence of peak temperature during in-service welding of API X70 pipeline steels on microstructure and fracture energy of the reheated coarse grain heat-affected zones. *J Mater Sci* 19:6424–6431. doi:10.1007/s10853-011-5592-7
40. Zhu Z, Kuzmikova L, Li H, Barbaro F (2014) Effect of inter-critically reheating temperature on microstructure and properties of simulated inter-critically reheated coarse grained heat affected zone in X70 steel. *Mater Sci Eng A* 605:8–13. doi:10.1016/j.msea.2014.03.034

41. Mandal M, Poole W, Militzer M, Collins L (2021) Mechanical properties of intercritically annealed X80 line pipe steels. *Metall Mater Trans A* 52:1336–1352. doi:10.1007/s11661-021-06152-5
42. Kostin VA, Grigorenko GM, Poznyakov VD (2020) Structural transformations of the metal of of heat-affected zone of welded joints of high-strength armor steels. *J Mater Sci* 55:78–83. doi:10.1007/s11003-020-00380-7
43. Ramachandran DC, Moon J, Lee CH, Kim SD, Chung JH, Biro E, Park YD (2021) Role of bainitic microstructures with MA constituent on the toughness of an HSLA steel for seismic resistant structural applications. *Mater Sci Eng A* 801:140390. doi:10.1016/j.msea.2020.140390
44. Kumar S, Nath SK (2016) Effect of weld thermal cycles on microstructures and mechanical properties in simulated heat-affected zone of a HY 85 steel. *Trans Indian Inst Met* 70:239–250. doi:10.1007/s12666-016-0880-1
45. Bayraktar E, Kaplan D (2004) Mechanical and metallurgical investigation of martensite–austenite constituents in simulated welding conditions. *J Mater Process Technol* 154:87–92. doi:10.1016/j.jmatprotec.2004.04.021
46. Li Y, Crowther DN, Green MJW, Mitchell PS, Baker TN (2001) The effect of vanadium and niobium on the properties and microstructure of the intercritically reheated coarse grained heat-affected zone in low carbon steel. *ISIJ international* 41:46–55. doi:10.2355/isijinternational.41.46
47. Mohammadjoo M, Kenny S, Collins L, Henein H, Ivey DG (2017) Characterization of HAZ of API X70 microalloyed steel welded by cold-wire tandem submerged arc welding. *Metall Mater Trans A* 48:2247–2259. doi:10.1007/s11661-017-4041-x

## Figures

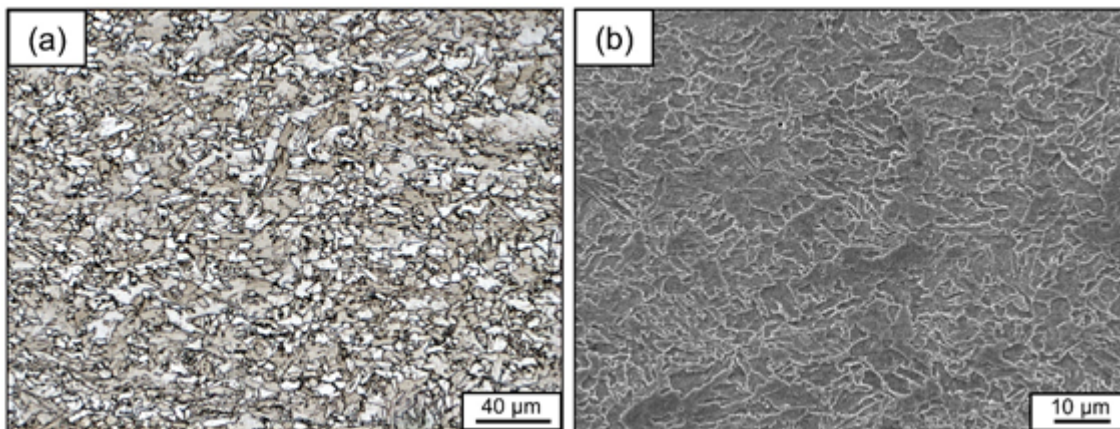


**Figure 1**

Optical (a) and scanning electron (b) micrographs of the fine-grained ferritic steel API 5L X70 pipe.

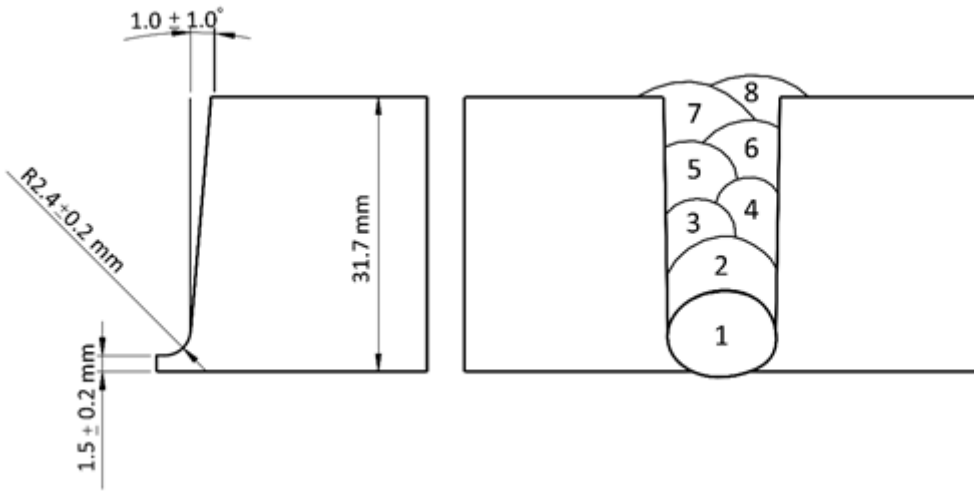


Figure 2

Groove configuration (left) and schematic of the weld pass sequence (right).

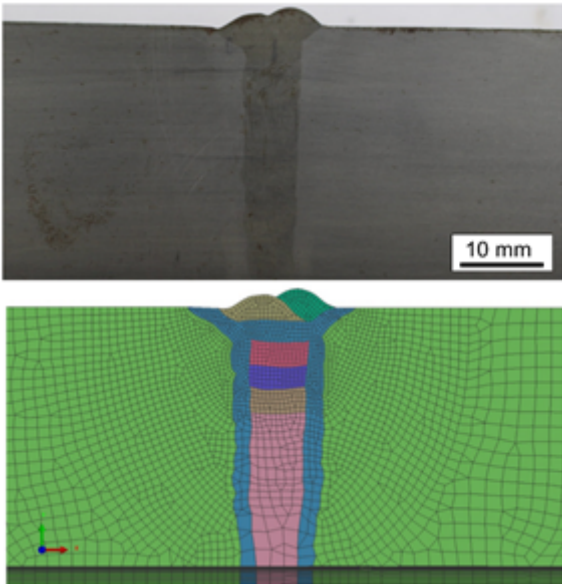


Figure 3

Macrograph of the welded joint (top) and the finite element method model mesh (bottom).

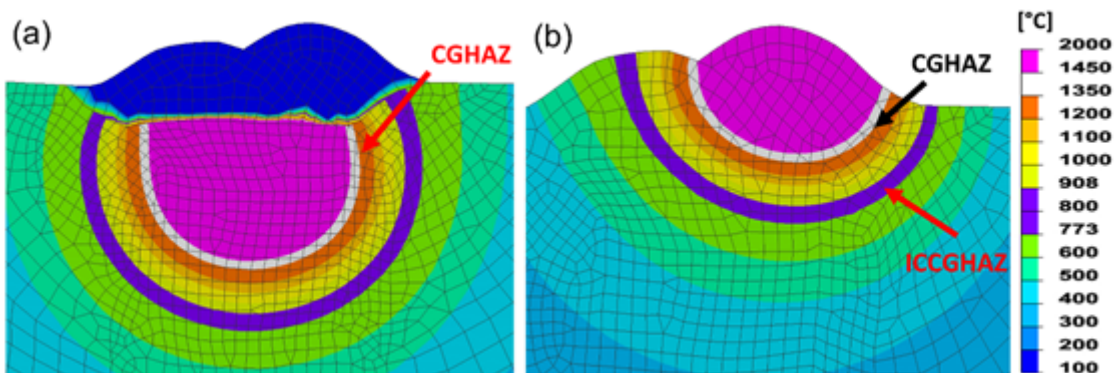
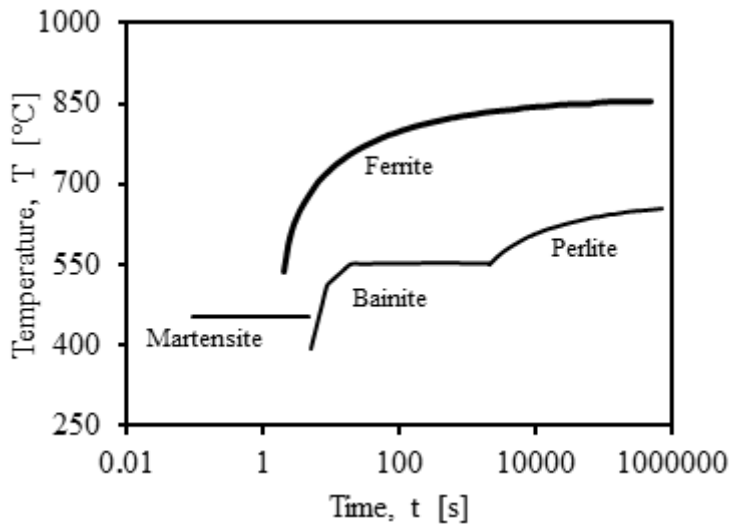


Figure 4

Thermal profile of the simulated welded joint. Simulation of the fifth and sixth weld pass forming the (a) coarse grain heat-affected zone (CGHAZ); and the seventh and eighth weld pass forming the (b) CGHAZ and intercritically reheated coarse-grain HAZ (ICCGHAZ).



**Figure 5**

Simulated API 5L X70 pipe continuous cooling transformation diagram.

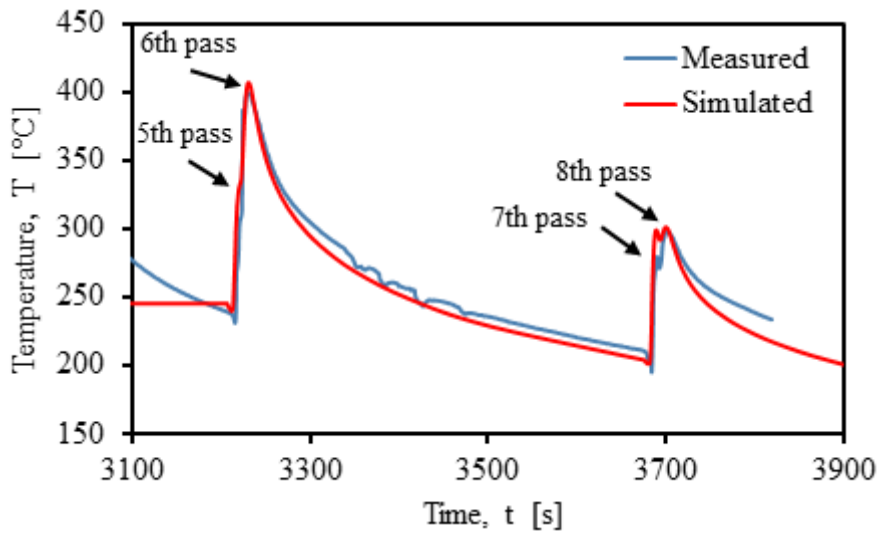


**Figure 6**

Welding thermal cycles measured with thermocouples and simulated with the commercial FEM software Sysweld®, both in the base metal 25 mm away from the joint groove.

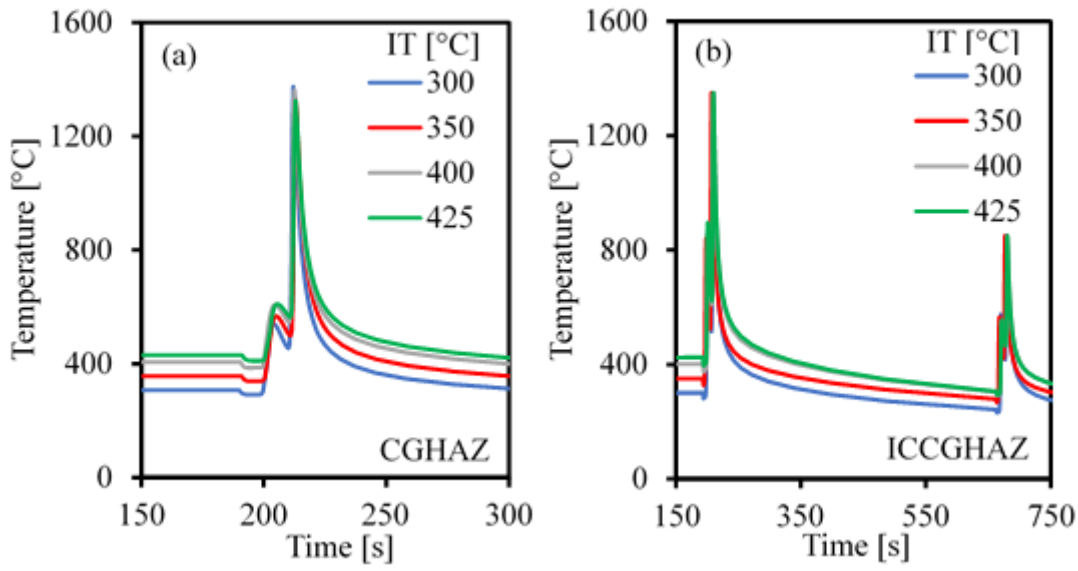


**Figure 7**

Simulated welding thermal cycles in the (a) coarse grain heat-affected zone (CGHAZ) and (b) intercritically reheated coarse-grain HAZ (ICCGHAZ) for different interpass temperatures (IT)

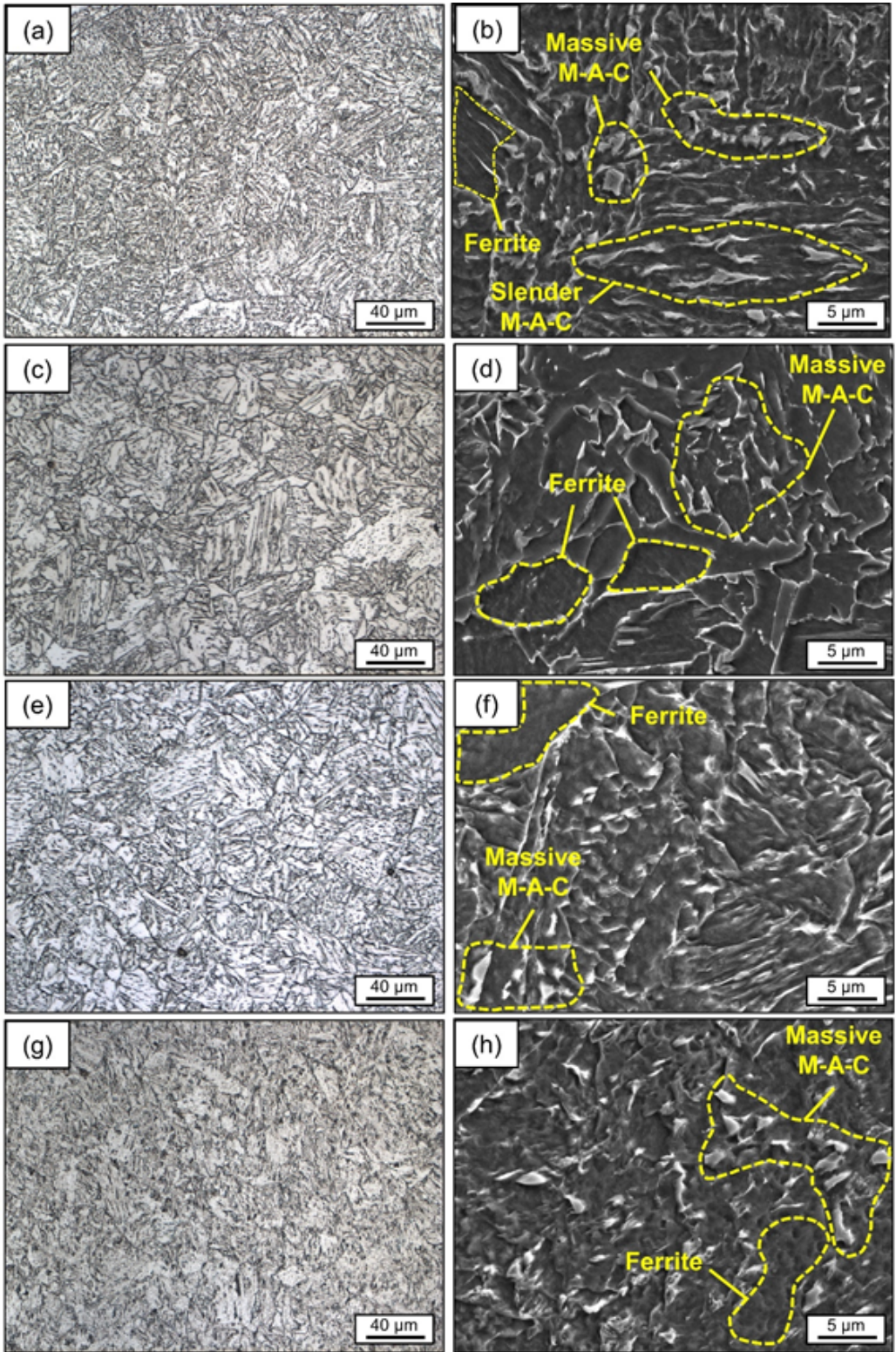


**Figure 8**

Optical (left) and scanning electron (right) micrographs of the simulated coarse grain heat-affected zone for the following interpass temperatures: (a) 300 °C, (b) 350 °C, (c) 400 °C, and (d) 425 °C.

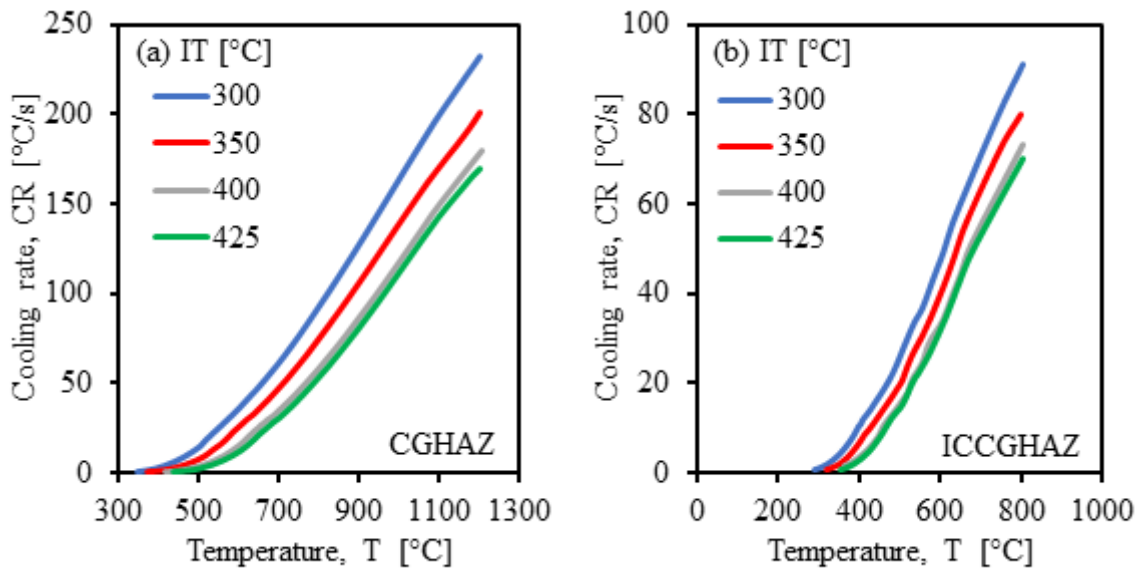


**Figure 9**

The coarse grain heat-affected zone (CGHAZ) (a) and intercritically reheated coarse-grain HAZ (ICCGHAZ) (b) cooling rates for interpass temperatures (IT) of 300, 350, 400, and 425 °C.

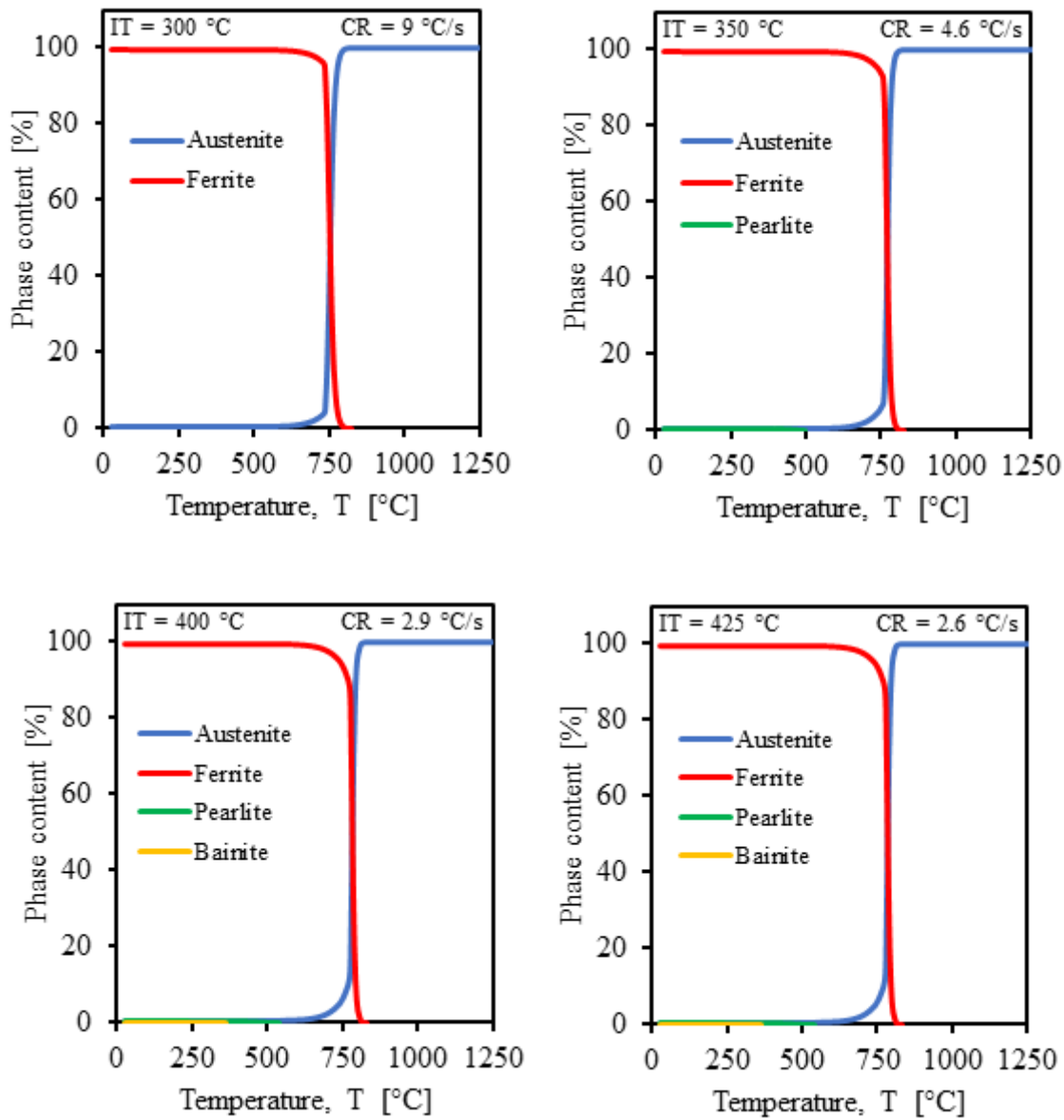


**Figure 10**

Simulated phase contents of the coarse grain heat-affected zone during cooling for interpass temperatures (IT) of 300, 350, 400, and 425 °C. CR means cooling rate.

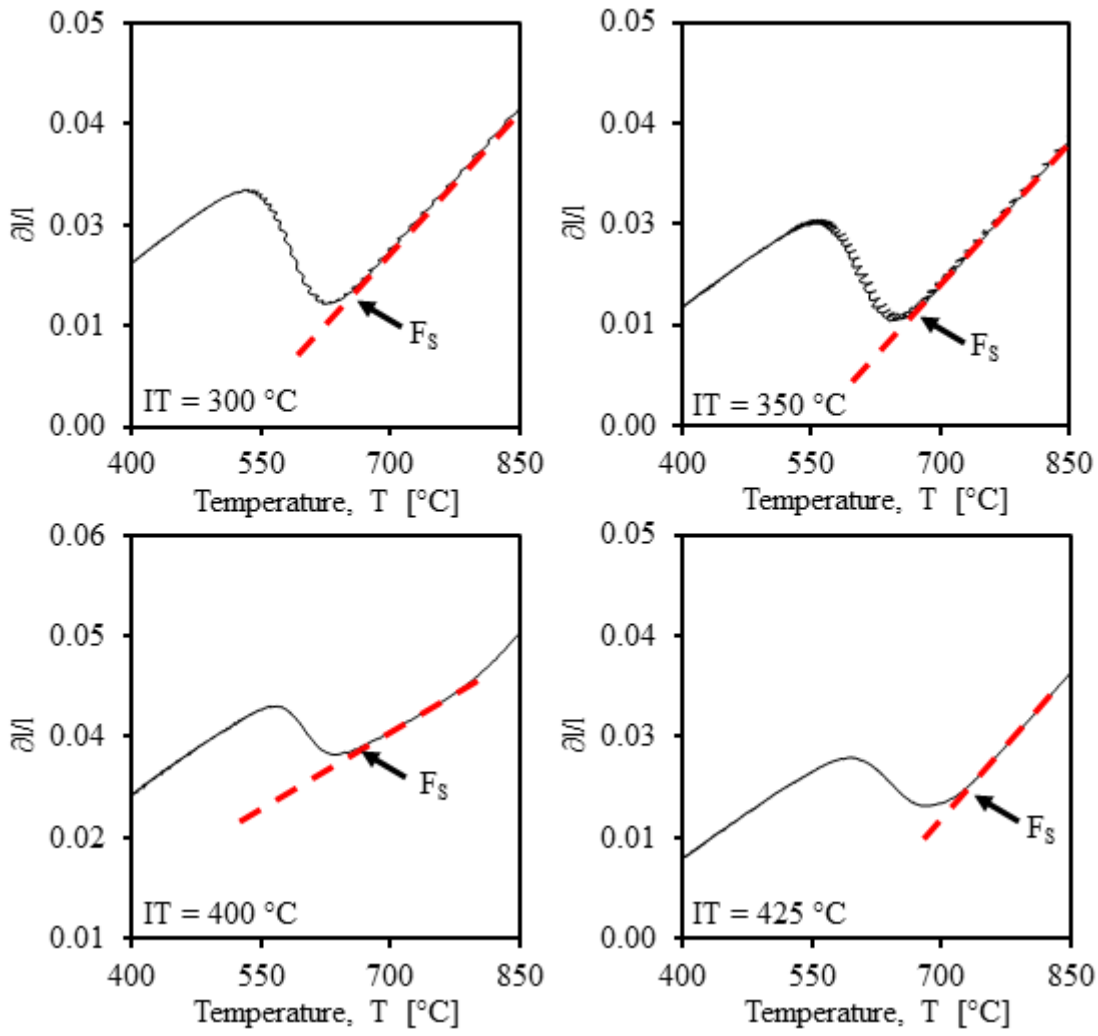


**Figure 11**

Results of the dilatometry test for the coarse grain heat-affected zone indicating the starting temperature of ferrite formation (FS) for all interpass temperatures (IT).

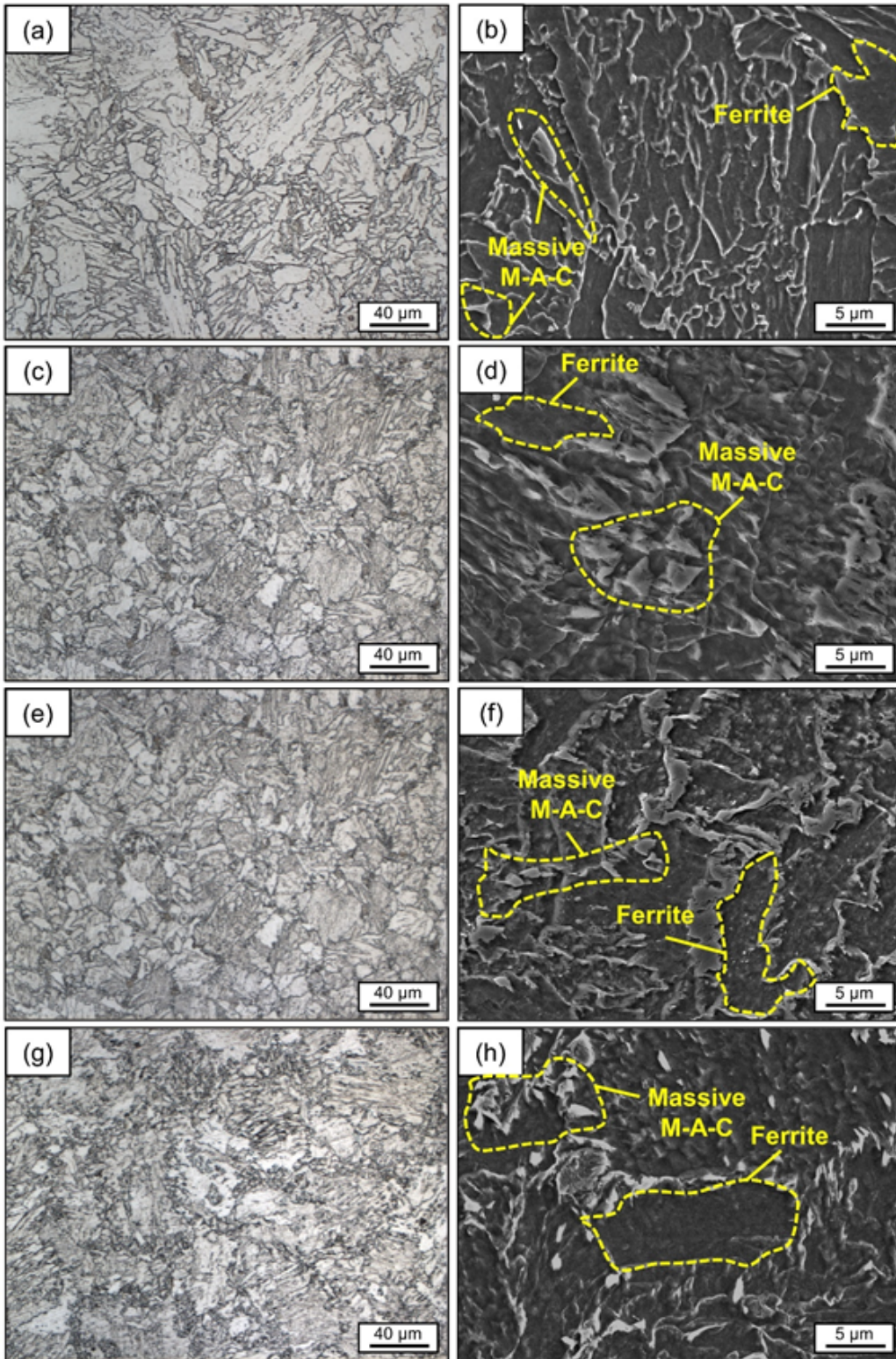


**Figure 12**

Optical (left) and scanning electron (right) micrographs of simulated intercritically reheated coarse-grain HAZ (ICCGHAZ) for interpass temperatures (IT) of (a) 300 °C, (b) 350 °C, (c) 400 °C, and (d) 425 °C.

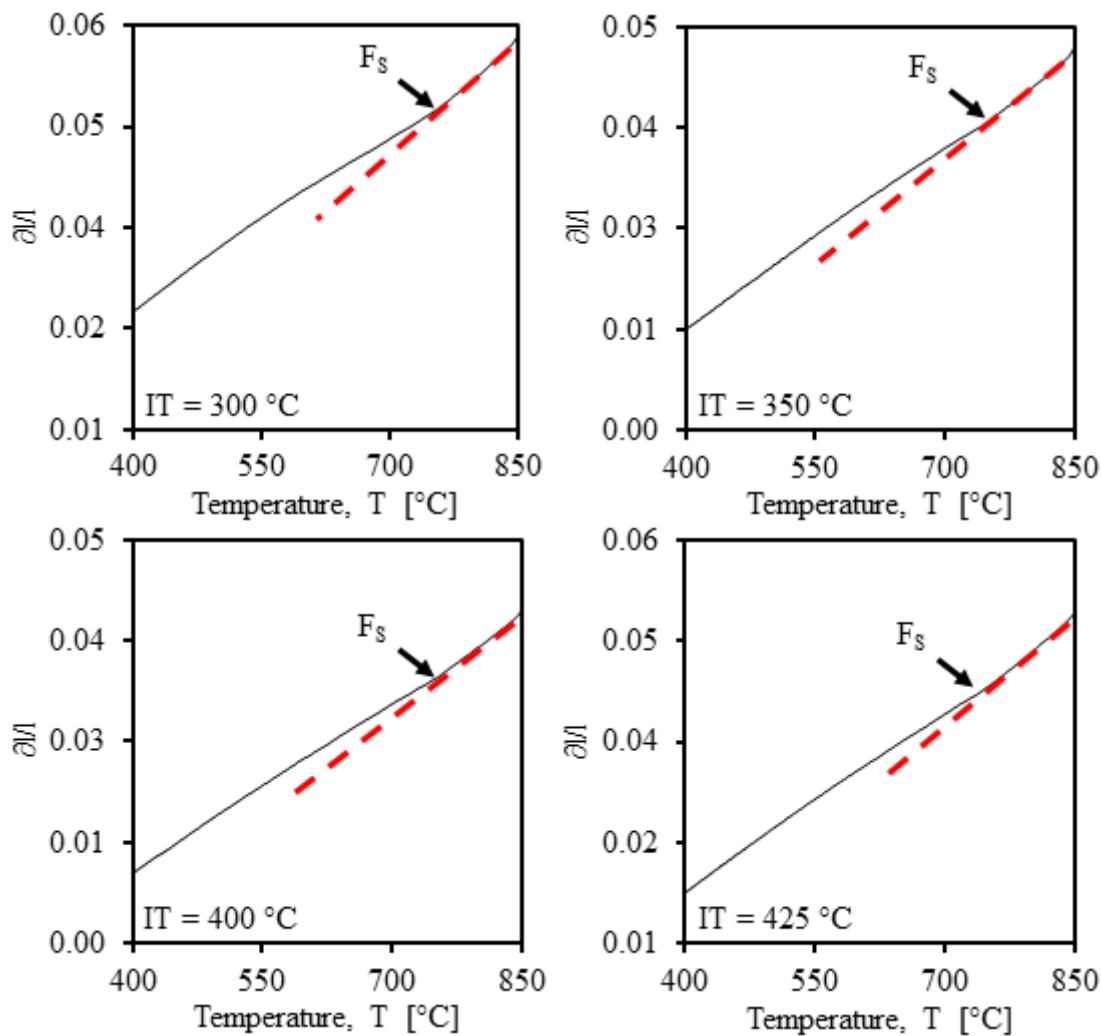


**Figure 13**

Results of the dilatometry test indicating the starting temperature of ferrite formation ( $F_s$ ) for the intercritically reheated coarse-grain heat-affected zone.

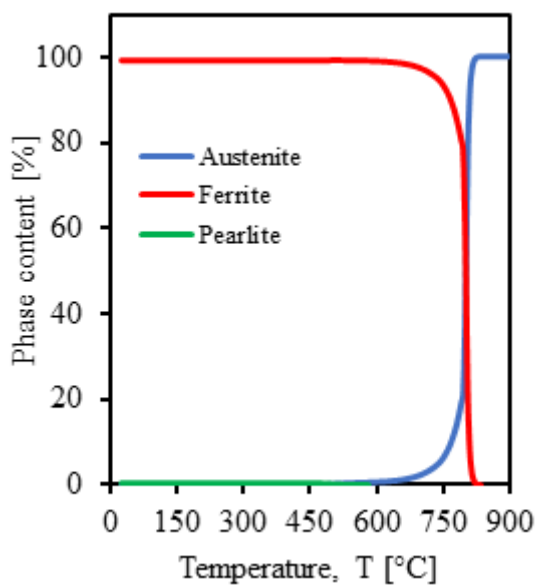


**Figure 14**

Simulated phase contents of the intercritically reheated coarse-grain heat-affected zone during cooling for all interpass temperatures (cooling rate = 1 °C/s).

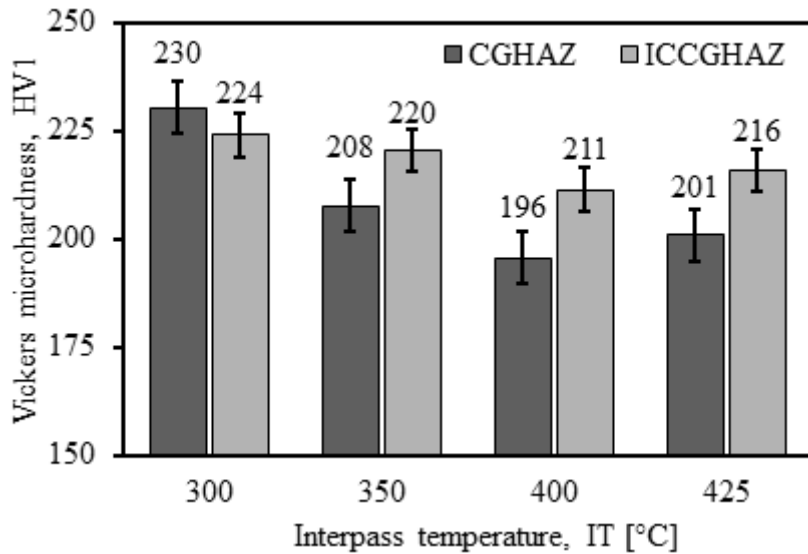


**Figure 15**

Vickers microhardness of the coarse grain heat-affected zone (CGHAZ) and intercritically reheated coarse-grain heat-affected zone (ICCGHAZ) for the interpass temperatures of 300, 350, 400, and 425 °C.